ADVANCED ENGINEERING MATERIALS
www.aem-journal.com

Improving the Defect Tolerance and Fatigue Strength of AM AlSi10Mg

Patrick Lehner, Bastian Blinn, and Tilmann Beck*

Additively manufactured structures reveal a poor surface quality and a high number of process-induced defects in the surface-near area, leading to a significant reduction of the fatigue strength. As laser-based powder bed fusion (PBF-LB) processes are used to produce topologically optimized lightweight structures with complex geometries, which cannot be fully machined, the influence of the process-induced surface on the fatigue behavior needs to be analyzed. For this, also the interrelation of the surface-induced notch effects with the surrounding material volume must be considered. As thermal treatments can also be applied to filigree components with complex geometries, in the presented work the influence of different heat treatments, i.e., stress relief annealing (SR) and artificial aging (T6), on the material properties, especially the defect tolerance, of AlSi10Mg manufactured via PBF-LB is analyzed. Both heat treatments lead to a dissolution of the cellular Si-rich network, resulting in decreased hardness and tensile strength, but higher fatigue strength. The increased fatigue strength results from a reduction of the process-induced residual stresses, but mainly a strongly improved defect tolerance. Consequently, to evaluate the fatigue strength of additively manufactured materials, besides the materials strength and the process-induced defects, also the defect tolerance must be considered.

1. Introduction

Additive manufacturing (AM) enables the fabrication of topologically optimized lightweight structures with complex geometries, increasing the efficiency of technical systems. However, the fatigue strength of additively manufactured components, even with smooth geometry, is reduced by process-induced notch effects, and their interaction with the residual stress state generated during the AM process.[1–4]

Notch effects are caused by the relatively high surface roughness[2,4] and microstructural defects,[3,5,6] which are often located in the surface-near area.[7–9] The impact of stress concentrations caused by process-induced defects on the fatigue life depends on the defect size and its position relative to the surface.[4,6,10] Thus, larger defects and defects at the surface cause higher stress concentrations, leading to a more pronounced decrease in the fatigue strength.[5,11] Moreover, also the relatively rough surface topography leads to stress concentrations, and hence to a reduced fatigue life.[4,6] As these process-induced notch effects cannot be avoided completely in additively manufactured materials, their influence on the fatigue strength must be analyzed thoroughly and considered for dimensioning.

Regarding the influence of process-induced defects on the fatigue life, the $\sqrt{\text{area}}$ approach established by Murakami[6] can be used, which considers the size and the location of the crack-initiating defect, as well as the hardness of the surrounding material.[6] Using this approach, the theoretical fatigue strength of a specimen can be determined depending on the defect size and position, which was applied in many research works on the fatigue behavior of additively manufactured metallic materials.[12–16] So Tenkamp et al.[17,18] combined this approach with the approach of Shiozawa[19] to calculate defect-based lifetime curves, which enables a reliable lifetime estimation in the HCF regime for Al–Si alloys.

Note that this work focuses on short crack propagation from preexisting defects evaluated by the $\sqrt{\text{area}}$ approach established by Murakami[6] and analyses the effect of defect-induced stress concentrations on the fatigue strength of different material properties. In this context, it should be considered that the fatigue life not solely depends on the defect size and position but also on the sensitivity of the surrounding material against the stress concentration induced by a defect, i.e., the defect tolerance. Based on the relation of the theoretical fatigue strength determined by means of the $\sqrt{\text{area}}$ approach and the stress amplitude applied in the fatigue test, the defect tolerance of the material can be evaluated.[13] As demonstrated by Kramer et al.[20] and in previous own work,[13,21,22] also cyclic indentation tests can be used to rate the defect tolerance of a material. By analyzing the cyclic deformation behavior obtained in instrumented cyclic indentation tests (CIT), the cyclic hardening potential of a material can be characterized, which qualitatively correlates with the defect tolerance.[13,22]

P. Lehner, B. Blinn, T. Beck
Institute of Materials Science and Engineering
RPTU Kaiserslautern-Landau
Gottlieb-Daimler-Straße, Gebäude 44, 67663 Kaiserslautern, Germany
E-mail: lehner@mv.uni-kl.de

The ORCID identification number(s) for the author(s) of this article can be found under https://doi.org/10.1002/adem.202201855.

DOI: 10.1002/adem.202201855

Because of the influence of the process-induced notch effects described earlier, an increase in fatigue strength can be achieved by reducing the defect size and/or surface roughness, or by improving the ability of the additively manufactured material to withstand local stress concentrations. These stress concentrations can occur at geometrical notches, material damages, and at relatively small process-induced defects, which can be treated equivalent to short cracks.[6] The ability of the material to withstand such stress concentrations caused by process-induced defects is further called "defect tolerance" and can be differentiated to the term "damage tolerance," which additionally comprises the stress concentrations occurring at bigger inhomogeneities, e.g., at geometrical notches or long cracks. In this context, machining of additively manufactured surfaces reduces process-induced surface notch effects, leading to a significantly higher fatigue strength.[15,23,24] However, the additively manufactured surfaces cannot be machined completely at filigree structures or components with complex geometries. In contrast, an improvement of the defect tolerance can be achieved by thermal treatments, which modify the material properties and can be applied independent on the geometry of the part. Accordingly, Aboulkhair et al.[25] and Bagherifard et al.[26] report an increase in fatigue strength after a T6 heat treatment of additively manufactured AlSi10Mg, which is explained by a higher ductility, correlating with a higher defect tolerance.

Besides changes in the mechanical properties, heat treatments can also reduce process-related residual stresses, and thus increase the fatigue strength.[27] In this context, Tridello et al.[27,28] reported a higher fatigue strength of additively manufactured AlSi10Mg after stress-relief annealing at 244 °C for 2 h due to a reduction of the process-induced tensile residual stresses at the surface. Moreover, Di Giovanni et al.[29] show that compressive residual stresses can be generated in the surface-near area by a T6 heat treatment, which is also beneficial for the fatigue strength and underlines the high potential of thermal treatments to improve the fatigue strength of additively manufactured AlSi10Mg.

To exploit the whole potential of thermal treatments for an improvement of the fatigue strength, their influence on the microstructure, the resulting defect tolerance and the residual stresses must be understood thoroughly. Moreover, the beneficial impact of the improved defect tolerance as well as the reduction of the tensile residual stresses at the surface must be determined. For this, in the presented work, two common heat treatments for additively manufactured AlSi10Mg, i.e., artificial aging (T6) and stress-relief heat treatment (SR), were applied on fatigue specimens manufactured via laser-based powder bed fusion (PBF-LB). Analyzing these heat-treated conditions as well as the "as-built" condition, the influence of the heat treatments on the microstructure and the resulting fatigue strength was determined. Therefore, the changes in the defect tolerance and the residual stress state were considered. To investigate the influence of the notch effects caused by the additively manufactured surface as well as the process-induced residual stresses at the surface, the specimens were manufactured near-net shaped tested without removal of the additively manufactured surface.

2. Materials

In this work, specimens of AlSi10Mg manufactured by PBF-LB were investigated. For the PBF-LB process, a 3D Systems ProX DMP 320 device and the process parameters given in **Table 1** were utilized. To realize a relatively high surface quality, the contour was produced using two tracks with a higher volumetric energy density E_{vol} than used for the inner section. While the contour was manufactured with a unidirectional scanning direction, for the inner region, a bidirectional scanning strategy, which was rotated from layer to layer by 67°, was used. As this work focuses on the interrelation of process-induced notch effects and the properties of the material volume, and since the notch effects are most pronounced in the surface-near area, the fatigue specimens were manufactured near-net shaped and thus had an additively manufactured surface condition.

To exclude any influence of the support structure on the surface topography, the specimens were manufactured vertically, with layer planes perpendicular to the loading direction (see **Figure 1**).

Although all specimens were manufactured with the identical scanning strategy and process parameters, two different geometries of fatigue specimens were realized, as shown in Figure 1. This was done to analyze the volume effect on the defect size, without changing the parameters of the PBF-LB process. According to the reports of Berretta et al.,[30] these different geometries are supposed to result in differences in the maximum defect sizes. Note that the different geometries result in nearly identical surface topographies (see S_z in Table 3). Despite the identical S_z, bigger maximum defect sizes are assumed for

Table 1. Process parameters and resulting volumetric energy density (E_{vol}) used to manufacture the inner volume and the contour of the specimens.

Volume	P in W	t in µm	v in mm s^{-1}	h in µm		E_{vol} in J mm^{-3}
	300	30	1400	100		71
Contour	P in W	t in µm	v in mm s^{-1}	h_1[a)] in µm	h_2[b)] in µm	E_{vol} in J mm^{-3}
	270	30	550	75	235	102

[a)]Distance of the first track to the surface. [b)]Distance of the second track to the surface.

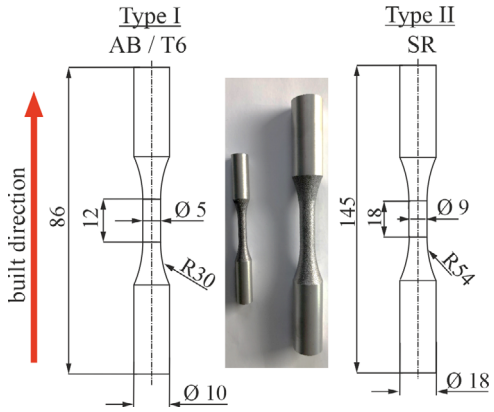

Figure 1. Geometries of the two different types of fatigue specimens investigated.

the specimen type II, due to their larger volume and the resulting higher probability of process-induced defects. Despite different geometries, no significant differences in thermal history were expected, as the dwell time between two layers was similar, and thus, the differences in defect sizes are assumed to be caused solely by the bigger volume.

Besides the different geometries, different powder batches with the same specification of sphericity and particle size distribution were used to manufacture the different types of specimens. However, as shown in **Table 2**, the chemical composition of both sample batches, which was determined by spectrophotometry on cross sections of the fatigue specimens, is nearly identical and only differs slightly in the Si content, which is considered neglectable.

To analyze the influence of the defect tolerance on the fatigue strength of additively manufactured AlSi10Mg and its interrelation with process-induced notch effects, different heat treatment conditions were investigated. Besides the "as-built" condition (AB), an artificially aged (T6) and a stress-relieved (SR) conditions were analyzed. For the artificial aging, the specimens were solution annealed at 530 °C for 2 h and then quenched in water. Subsequently, an aging at 160 °C was performed for 12 h. Afterward, the specimens were cooled in ambient air. The stress-relief heat treatment was conducted at 300 °C for 2 h followed by cooling in the furnace to avoid thermally induced residual stresses. While the artificially aged (T6) and "as-built" (AB) specimens had the geometry of type I, the stress-relief heat treatment was performed on the specimens of type II (see Figure 1) due to the fact that typically higher residual stresses evolve in bigger additively manufactured material volumes.

In accordance with Takata et al.,[31] the light optical micrograph of the "as-built" condition shown in **Figure 2**a reveals layer boundaries. At higher magnification, this condition exhibits a Si-rich cellular network (see Figure 2a,b), which corresponds to the works of Fousová et al.[32] and Wu et al.[33] As shown in Figure 2a, the layer structure in the surface-near area, being extended to a distance to the surface of roughly 250 µm, is slightly different to that in the inner volume. As this surface-near area is crucial for fatigue life, the microstructural images shown in Figure 2b,d,f were taken in this area for all conditions.

The additively manufactured microstructural features, i.e., the layer boundaries and the Si-rich cellular network, are dissolved after annealing and artificial aging. After the T6 heat treatment, the microstructure does not show any layer boundaries or intragranular cellular structures (see Figure 2e,f). In contrast to artificial aging, the stress-relief heat treatment does not resolve the layer structure, which can be observed in Figure 2c. This is assumed to be caused by the significantly smaller temperature, leading to less pronounced diffusion processes which are insufficient to dissolve the layer structure. However, the Si-rich cellular network of the SR condition is decomposed and shows coarser, nearly spherical Si particles (see Figure 2d), which is in accordance with the reports of Takata et al.[31] und Zhao et al.[34]

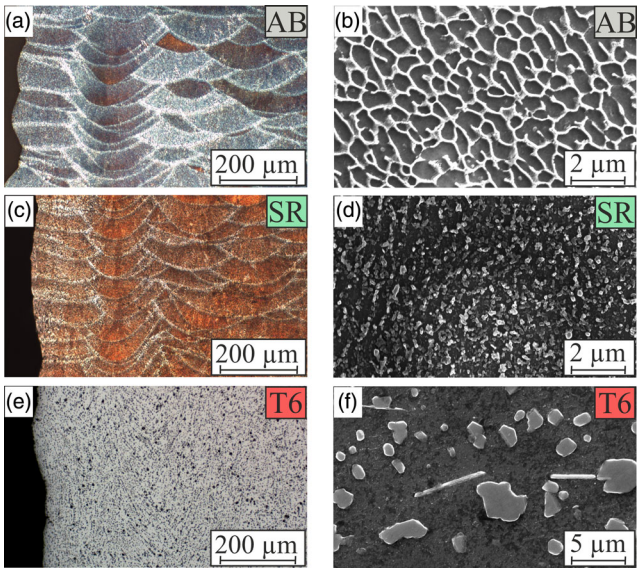

Figure 2. Light optical micrographs a,c,e) taken at longitudinal sections of the different conditions and respective scanning electron microscopy (SEM) images b,d,f) obtained in the surface-near area.

Besides the dissolution of characteristic additively manufactured microstructural features caused by the solution annealing, the artificial aging results in a formation of precipitates, as expected for a T6 treatment of AlSi10Mg. Note that these kinds of precipitates were not found in the other conditions at the magnifications shown in Figure 2b,d. To analyze this more thoroughly, high-resolution microscopy is required, which is the objective of future work.

In summary, the applied heat treatments led to pronounced variations in the microstructure, and thus, significant differences in the mechanical properties are assumed. Despite the microstructural changes, the heat treatments did not influence, the surface roughness (see **Table 3**), and hence, only the microstructure and material volume properties are changed by the heat treatments. The influence of the changes induced by the heat treatments on the monotonic and cyclic properties will be discussed in Section 4.

In addition to the microstructure, the porosity was analyzed by light optical microscopy. The results given in Table 3 show comparable porosity for all variants. Thus, the bigger specimen geometry of the SR specimens seems to result in similar average defect distribution.

Table 2. Chemical composition of the different specimen types made of AlSi10Mg in wt%.

	Si	Mg	Fe	Cu	Mn	Ni	Zn	Ti
Type I	10.026	0.273	0.122	0.004	0.003	0.006	0.005	0.010
Type II	9.923	0.280	0.141	0.004	0.003	0.006	0.004	0.010

Table 3. Maximum surface peaks S_z, porosity in the surface area $\varphi_{surf.}$, Vickers hardness HV, tensile strength R_m, 0.2% yield strength $R_{p0.2}$, and elongation at fracture a of the conditions investigated.

Condition	S_z in µm	$\varphi_{surf.}$ in %	HV_{10}	R_m in MPa	$R_{p0.2}$ in MPa	A in %
AB	107.3 ± 24	0.28 ± 0.23	129 ± 2	455 ± 15	233 ± 4	3.7 ± 1.0
SR	106.8 ± 25	0.14 ± 0.04	92 ± 1	286 ± 3	181 ± 4	11.6 ± 0.5
T6	106.9 ± 22	0.15 ± 0.13	98 ± 1	285 ± 4	234 ± 3	6.5 ± 1.0

3. Experimental Methods

The microstructural characterization was conducted at cross and longitudinal sections extracted from the gauge sections of unloaded fatigue specimens. To visualize the microstructure, the samples were ground, mechanically polished, and subsequently etched with 5% NaOH for 30 s. The microstructural images were taken with a Leica 6000 DM light optical microscope and an FEI Quanta 600 scanning electron microscope (SEM) using an acceleration voltage of 20 kV.

To characterize the surface topography of the fatigue specimens, a confocal microscope NanoFocus μSurf explorer with an objective 800 XS was utilized. The confocal microscopy analyses were performed at two specimens for each condition, using a 20× zoom factor and an aperture of 0.60. To analyze the specimens of type I, along the circumference areas of 1 mm × 1.5 mm were measured in 45° steps in the middle of the gauge length, while for type II areas of 1.2 mm × 1.58 mm and 72° steps were used. Based on the overall measurement data, the maximum height S_z was determined according to DIN EN ISO 25 178-2 for each condition.[35]

To analyze the initial porosity of the different specimens two cross and longitudinal sections were examined using light optical microscopy. For each section, four images were taken from the surface area with a surface distance of 500 μm. The evaluation of porosity was carried out using the image analysis software IMS from IMAGIC.

Using a Zwick/Roell ZHU250 tabletop device, the Vickers hardness HV_{10} was determined based on a minimum number of six indentation points distributed over two cross sections for each condition. Additionally, tensile tests were performed at each material condition in strain control according with DIN EN ISO 6892-1, using a Zwick/Roell Z250 electromechanical testing device equipped with a fine gage extensometer and rotationally symmetric specimens.[36] In accordance with the DIN EN ISO 6892-1, the strain rate used in the elastic regime of the stress–strain curve was $\dot{\varepsilon} = 0.00025$, while after exceeding the elastically dominated regime the strain rate was defined to be $\dot{\varepsilon} = 0.0067$.

While for the AB and T6 conditions, specimens with a gauge section diameter of 8 mm and an initial gauge length of 48 mm were used, and the tensile tests at the SR condition were performed on specimens with a gauge section diameter of 10 mm and an initial gauge length of 60 mm.

To analyze the influence of the heat treatments and the resulting microstructural changes on the fatigue behavior, uniaxial fatigue tests were conducted at ambient temperature. The fatigue tests were performed stress controlled on a servo-hydraulic test system Schenck PSA 10 kN, using a sinusoidal load function with a stress ratio of $R = -1$ and a frequency of $f = 10$ Hz. The fatigue tests were carried out in the HCF regime, whereby the ultimate number of cycles was defined at 10^7. Depending on the material condition, stress amplitudes in the between 40 and 160 MPa were applied in the fatigue tests.

As the focus of this work was the influence of the heat treatment on the defect tolerance, the fracture surfaces were analyzed using SEM to investigate the respective crack-initiating defects. Based on the fracture surface analyses, for each specimen the size of the crack-initiating defect was determined using the $\sqrt{\text{area}}$ approach established by Murakami.[6] For shallow surface defects, which had a ratio of the length l to the depth c higher than 10, the value of $\sqrt{\text{area}}$ was determined according to Murakami[6] with Equation (1).

$$\frac{l}{c} > 10: \quad \sqrt{\text{area}} = \sqrt{10}\, c \tag{1}$$

Based on the size of the crack-initiating defect and the Vickers hardness HV measured, the theoretical fatigue strength $\sigma_{w,\ Nog.}$ was calculated for each specimen using Equation (2). Here, C_M is a constant depending on the defect classification according to Murakami,[6] i.e., $C_M = 1.43$ for surface defect, $C_M = 1.56$ for internal defect and $C_M = 1.41$ for an inner defect with contact to the surface. Note that Equation (2) includes the modification proposed by Noguchi et al.,[37] which enables to apply the relations found for steels by Murakami[6] on nonferrous metallic materials. Therefore, in the present work the ratio of the Young`s moduli of Aluminium E_{Al} and steel $E_{st.}$ is required. As proposed by Noguchi et al.[37] $E_{st.}$ was defined to be 210 GPa, while for the material conditions investigated in this work E_{Al} was assumed constant as 70 GPa.

$$\sigma_{w,\,Nog.} = \frac{C_M(\text{HV} + 120 \cdot \frac{E_{Al}}{E_{St}})}{(\sqrt{\text{area}})^{\frac{1}{6}}} \tag{2}$$

Besides the influence of defects, the impact of the process-induced residual stresses was considered. Therefore, for all conditions the type I residual stresses at the surface of the gauge length were determined using X-ray diffraction (XRD). Therefore, the $\sin^2\psi$ method was applied using 8 different ψ angles from –69.30° to +69.30° on the diffraction peak of the (2 2 0) α-aluminium lattice plane. The XRD measurements were conducted on a laboratory diffractometer (Malvern Panalytical) using a Cu-$K_{\alpha 1}$ radiation accelerated with 40 kV and 40 mA, and a spot size of 1.5 mm × 1.5 mm. The scanning parameters were defined within the range of $62.70° < 2\theta < 67.70°$ with a scanning speed at $0.005° \text{ s}^{-1}$. Note that in this work only the residual stresses parallel to the building and hence, to the loading direction are considered.

To evaluate the influence of residual stresses on the fatigue strength, a further modification of Equation (2) was used to determine $\sigma_{w,\ Nog.}$ by considering the stress ratio R. Therefore, Equation (3) was used in accordance with Murakami[6] and Noguchi et al.,[37] whereby α was determined using Equation (4), which considers the materials sensitivity against mean stresses. Note that the residual stresses were supposed to act like mean stresses, and thus, the stress ratio R was modified by the value of the corresponding residual stresses of each condition.

$$\sigma_{w,Nog.} = \frac{C_M\left(HV + 120 \cdot \frac{E_{Al}}{E_{St}}\right)}{(\sqrt{\text{area}})^{\frac{1}{6}}} \left(\frac{1-R}{2}\right)^{\alpha} \tag{3}$$

$$\alpha = 0.226 + \text{HV} \cdot 10^{-4} \tag{4}$$

In addition to these analyses, the cyclic hardening potential of the different material conditions was evaluated by using instrumented cyclic indentation tests (CIT). The CIT were performed with a Fischerscope H100C device from Helmut Fischer GmbH equipped with a Vickers indenter. For cyclic indentation, a

sinusoidal load function with a maximum indentation force of 200 mN and a frequency of 1/12 Hz was used. During the ten cycles applied in the CIT, the indentation force F and the indentation depth h were measured continuously, resulting in an F–h hysteresis from the second cycle onward(compare **Figure 3**a). In analogy to the plastic strain amplitude obtained from a stress–strain hysteresis, the half width of the F–h hysteresis at mean loading is defined as the plastic indentation depth amplitude $h_{a,p}$. Hence, the change in $h_{a,p}$ during the ten cycles, which is called $h_{a,p}$-N curve (see Figure 3b), can be used to characterize the cyclic deformation behavior. Moreover, from the fifth cycle onward, the $h_{a,p}$-N curves show a stabilized slope, indicating a saturation of microplastic deformation processes, i.e., domination of cyclic microplasticity. This regime of the $h_{a,p}$-N curve can further be expressed by the power function given in Equation (5)

$$5 \leq N \leq 10: \quad h_{a,p\,II} = a_{II} \cdot N^{e_{II}} \tag{5}$$

Note that the cyclic hardening exponent$_{CHT}$ e_{II} describes the slope of the $h_{a,p}$-N curve in the stabilized regime. The steeper the slope of the $h_{a,p}$-N curve in this region, the more pronounced are the cyclic hardening processes that occur during cyclic indentation. Accordingly, a higher $|e_{II}|$ indicates a higher cyclic hardening potential of the material,[20,21] which correlates to the ability to counteract locally increased stresses, e.g., at microstructural defects, and thus with the defect tolerance.[13,22] Furthermore, the first indentation cycle can be used to determine the Martens hardness (HM), which enables an evaluation of the local monotonic properties. This approach is called PhyBaL$_{CHT}$ and is presented in more detail in previous work.[20,21]

In the presented work, the CIT were conducted on mechanically polished cross sections extracted from the gauge lengths of unloaded fatigue specimens at a distance to the surface of 50 µm (see Figure 3c). As in this work the crack initiation started solely from the surface, for an evaluation of the material surrounding the crack-initiating defects, the CIT must be performed in this region. To ensure a sufficient statistical reliability of the results obtained, 40 CIT were performed for each condition investigated.

4. Results

4.1. Monotonic Properties

As shown in Section 2, the applied heat treatments led to significant variations in the microstructure. As a basis for the analysis of the fatigue behavior, the monotonic properties resulting from these different microstructures were investigated using hardness measurements and tensile tests. The values given in Table 3 show that both heat treatments led to a significant decrease in hardness and tensile strength R_m, whereas the SR and T6 conditions reveal nearly identical R_m and only slightly different HV.

However, considering the stress–strain curves (see **Figure 4**) and 0.2% yield strengths $R_{p0.2}$ (see Table 3) obtained in tensile tests, the T6 condition shows pronounced differences to the stress-relieved specimens. After artificial aging, $R_{p0.2}$ is significantly higher compared to the SR condition. Because of artificial aging, the T6-treated sample shows the smallest strain hardening rate, resulting in nearly identical R_m as found for the SR

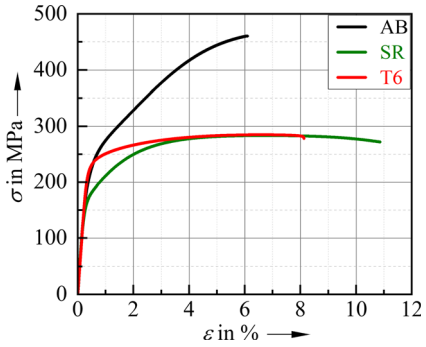

Figure 4. Stress–strain curves obtained in tensile tests at the different conditions investigated.

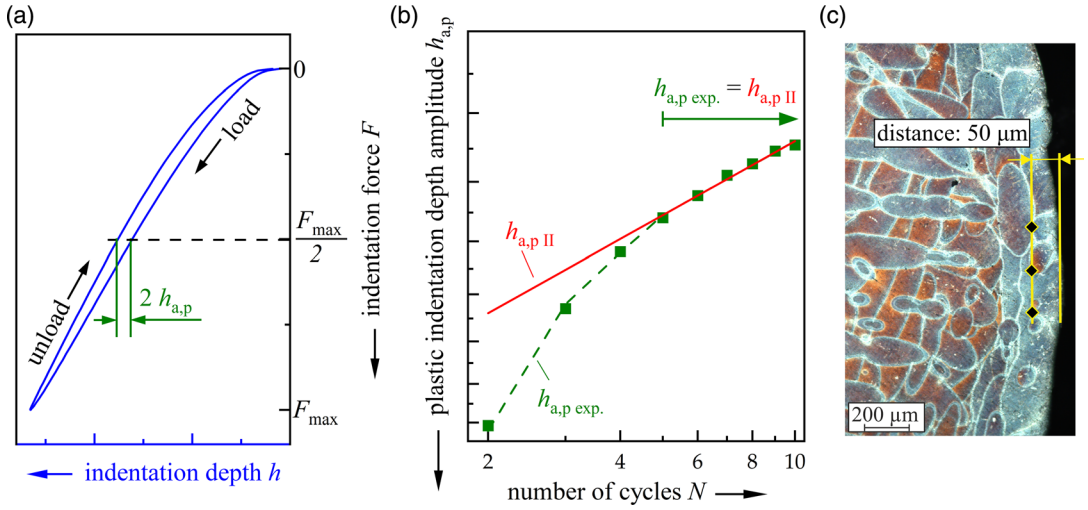

Figure 3. Schematic of a) the F-h hysteresis as well as a b) the $h_{a,p}$-N curve and c) illustration of the position of the indentation points in the surface-near area.

specimens. Furthermore, the T6 condition reveals similar $R_{p0.2}$ as the "as-built" variant, while the "as-built" specimens show the most pronounced strain hardening, and thus the highest tensile strength.

Besides the highest hardness, the "as-built" condition has the lowest ductility, indicated by the smallest elongation at fracture *A*, while the stress-relief heat treatment results in the biggest *A* and hence highest ductility.

The differences observed in the monotonic properties are related to the microstructural observations illustrated in Figure 2. The significantly higher strength of the "as-built" condition can be explained by the cellular Si rich network, providing strong obstacles for dislocation movement.[38] This cellular microstructure further results in a brittle behavior and hence a small elongation at fracture *A*. This is underlined by the respective values found for the SR condition which has no intragranular cell structures. This results in a significant decrease in monotonic strength but a highly improved ductility.

As the T6 condition also has no cellular structure, the artificially aged specimens yield higher *A* but smaller R_m than the "as-built" condition. However, when compared to the SR condition, the precipitates formed due to the T6 treatment result in an increased 0.2% yield strength, which is accompanied with a decrease in ductility.

Considering the strength and ductility obtained for the different conditions, a high-strength (AB), a highly ductile (SR) condition, and a compromise of these properties (T6) resulted from the applied heat treatments. As shown by Leuders et al.,[39] the strength and the ductility determine the fatigue strength of additively manufactured materials, and thus, significant variations in the fatigue behavior are expected, which are analyzed in the following section.

4.2. Fatigue Behavior of the Differently Heat-Treated Conditions

To analyze the fatigue behavior that results from the different microstructures, Woehler curves were determined for each condition, being illustrated in **Figure 5**a. Despite the highest hardness and R_m, the "as-built" condition has the lowest fatigue strength, while the T6 heat treatment results in the highest fatigue strength. This indicates that the improved ductility increases the fatigue life, which corresponds to the fatigue strength obtained for the SR condition, being also significantly higher in relation to the "as-built" condition.

As the fatigue strength of additively manufactured AlSi10Mg strongly depends on process-induced defects,[2,27,40] the fracture surfaces were analyzed. In the fracture surfaces, crack initiation at process-induced surface defects was observed for all investigated specimens. This is illustrated in Figure 5b–d, showing representative crack initiation sites for each condition. To investigate whether differences in the size of the crack-initiating defect led to the differences in the Woehler curves, the distribution of the defect sizes was determined for each condition, as shown in **Figure 6**. The size distribution of the crack-initiating defects is similar for the T6 and "as-built" conditions, and thus, the differences observed in the Woehler curves are caused by changes in the material properties induced by the T6 heat treatment. That these conditions show identical defect sizes is reasonable, as these specimens were produced using the same powder batch, process parameters and geometry.

Compared to the crack-initiating defects of the AB and T6 condition, the SR specimens show bigger crack-initiating defects and a larger scatter. This is in contrast with the nearly similar porosity obtained by light optical microscopy and the nearly identical

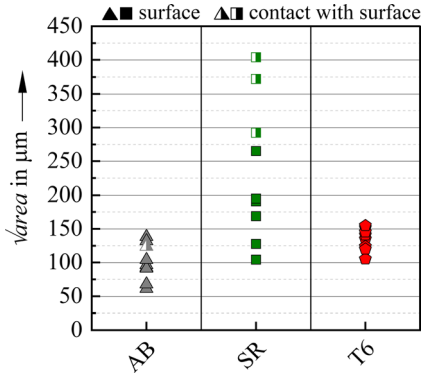

Figure 6. Size distributions of the crack-initiating defects (represented by $\sqrt{area}$) for the different conditions investigated.

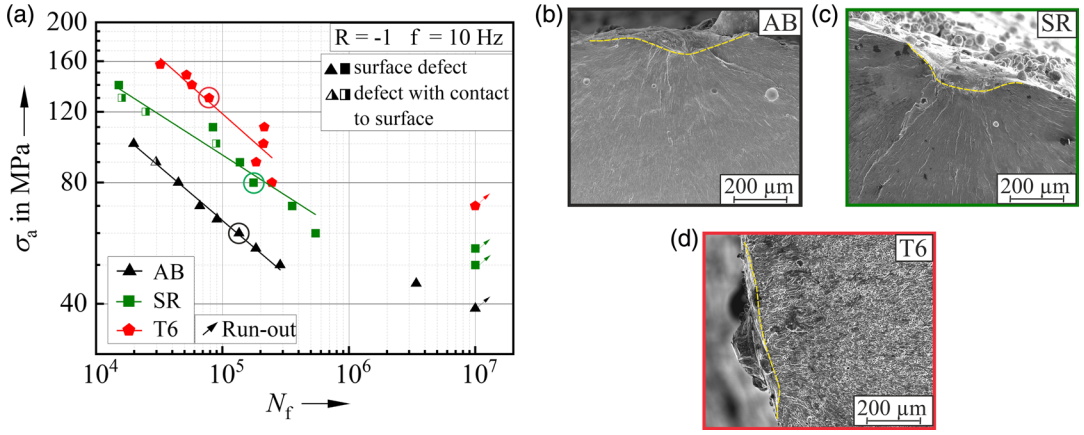

Figure 5. a) Woehler curves of the differently heat-treated specimens as well as representative crack initiation sites of the b) "as-built" (AB), c) stress-relieved (SR), and d) artificially aged (T6) condition.

surface roughness (see Table 3). Thus, it is assumed that the bigger crack-initiating defects are attributed to the larger volume of the SR specimen, which increases the probability of forming bigger process-induced defects, as also reported by Beretta et al.[30] This is further supported by the defect size of 100 µm observed for one SR specimen, which is in the range of the other conditions. Since in case of HCF loadings fatigue cracks usually are initiated at the most critical defects, the bigger defects observed for the SR condition are not present in all specimens, further supporting the assumption, that these bigger defects are an outcome of statistical size effect. Note that every crack-initiating defect observed was classified as surface defect or defect with contact to the surface, and, hence, no specimen failed due to internal defects.

Although the SR specimens have a lower hardness and bigger defects, they show a higher fatigue life than the "as-built" specimens, which is a consequence of the increased ductility of the material volume.

Comparing the SR and T6 conditions, the higher fatigue life of the T6 heat-treated specimens might be caused by the smaller defect sizes but can also result from the higher strength caused by the precipitates.

The Woehler curves indicate that an improved ductility increases the fatigue life in the context of defect-based failure. However, the presented results are superimposed by the different sizes of the process-induced defects. Consequently, the influence of the defects is examined in the following section.

4.3. Analysis of the Influence of the Defect Tolerance on the Fatigue Life

As shown in Section 4.2, the crack initiation sites are located at process-induced defects. Considering the works of Beretta et al.,[30] Wu et al.[9] and Domfang et al.[41] on differently heat-treated AlSi10Mg manufactured via PBF-LB, the transition from short to long cracks is defined between 200 and 500 µm, while for stress-relief annealed specimens in the work of Wu et al.,[9] a transition at roughly 400 to 500 µm was reported. According to the definition of Zerbst et al.,[42] the defects observed in this work can hence be defined as short cracks. Thus, the $\sqrt{\text{area}}$ approach established by Murakami,[6] modified by Noguchi et al.[37] for nonferrous metals, was used to analyze the impact of the defects on the fatigue life. Using this approach, for each specimen, the relation of the stress amplitude applied σ_a and the theoretical fatigue strength based on the crack-initiating defect $\sigma_{w,\,Nog.}$ was determined, which represents qualitatively the stress intensity at the crack initiation site. As shown in other research works,[5,13,43] the quotient $\sigma_a/\sigma_{w,\,Nog.}$ is crucial for the number of cycles to failure N_f, and thus, modified Woehler curves, i.e., $\sigma_a/\sigma_{w,\,Nog.}$–$N_f$ curves can be determined, which are illustrated in **Figure 7**. For defect-dominated failure, $\sigma_a/\sigma_{w,\,Nog}$ and N_f reveal a strong correlation, which is demonstrated in Figure 7. Besides this strong correlation, some values of $\sigma_a/\sigma_{w,\,Nog.}$ are smaller than 1, which seems not to be reasonable, since stress amplitudes lower than the theoretical fatigue strength $\sigma_{w,\,Nog.}$ led to failure. However, all conditions show a high coefficient of correlation, and thus, these modified curves can be used for a qualitative comparison. The relatively low values of $\sigma_a/\sigma_{w,\,Nog.}$ are assumed

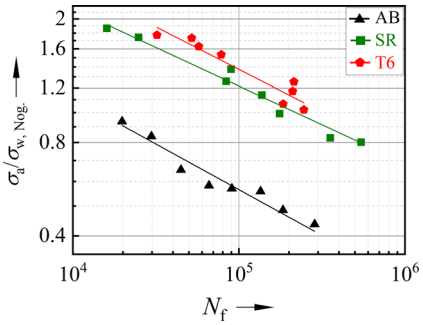

Figure 7. $\sigma_a/\sigma_{w,Nog.}$-N_f curves determined for the specimens of the different conditions investigated.

to be caused by the rough modification of Noguchi et al.[37] and were also shown in other research works.[43]

Note that a quantitative determination of the fatigue strength was not the aim of this work, which focuses on the evaluation of the defect tolerance. As $\sigma_{w,\,Nog.}$ depends on the defect size, the influence of the different sizes of crack-initiating defects is filtered in the $\sigma_a/\sigma_{w,\,Nog.}$-$N_f$ curves, which enables a comparison of the different conditions regarding their material volume properties. In this context, it should be noted that the difference in hardness and hence strength of the material volume is also considered in the $\sigma_a/\sigma_{w,\,Nog.}$-$N_f$ curves, since the Vickers hardness is used for the determination of $\sigma_{w,\,Nog.}$ Besides the influence of the defect size on the fatigue life, the $\sigma_a/\sigma_{w,\,Nog.}$-$N_f$ curves enable a qualitative evaluation of the defect tolerance of different materials.[13,22] If one material condition shows similar N_f at higher $\sigma_a/\sigma_{w,\,Nog.}$ in relation to another material condition, a higher defect tolerance is implied because it withstands a higher stress intensity for the same number of cycles.[13,22]

The smallest $\sigma_a/\sigma_{w,\,Nog.}$ are found for the "as-built" condition, which is in accordance with the conventional Woehler curves (see Figure 5a). Comparing the T6 and SR conditions, the difference in the respective $\sigma_a/\sigma_{w,\,Nog.}$-$N_f$ curves is less pronounced in relation to the conventional Wohler curves (compare Figure 5a and 7). This corresponds with the bigger defect sizes obtained for the SR condition, being considered in Figure 7. However, also in the $\sigma_a/\sigma_{w,\,Nog.}$-$N_f$ curves, the T6 conditions exhibit the highest fatigue life.

The $\sigma_a/\sigma_{w,Nog.}$-N_f curves in Figure 7 indicate a significantly increased defect tolerance after the heat treatments. This effect seems to be most pronounced after the T6 heat treatment, which shows the highest $\sigma_a/\sigma_{w,Nog.}$ However, in this context the process-induced residual stresses must be considered. From literature, it can be assumed that the additively manufactured surface exhibits tensile residual stresses,[16] which are supposed to be resolved after the heat treatments. Hence, the differences observed in the $\sigma_a/\sigma_{w,Nog.}$-N_f curves might also be caused by the respective residual stress state. To determine the influence of the residual stress state, the residual stresses at the surface were determined for each condition at unloaded fatigue specimens. The results are given in **Table 4**.

As expected, the AB condition shows relatively high tensile residual stresses, while the stress-relief heat treatment led to a nearly stress-free condition. In contrast, the T6 heat treatment

Table 4. Type I residual stresses parallel to the loading direction measured by X-ray diffraction at the surface in the gauge section of the fatigue specimens.

Condition	AB	SR	T6
Residual stress σ_{rs} in MPa	115.1 ± 8.0	8.7 ± 6.6	−43.0 ± 7.2

resulted in compressive residual stresses, which is assumed to be caused by the quenching after solution annealing.

These strong differences in the residual stress states can significantly influence the fatigue behavior. To determine how the residual stresses affect the $\sigma_a/\sigma_{w,Nog.}$–N_f curves, they were considered as mean stresses superimposed to the applied stress ratio R. Note that the residual stresses measured in the initial state can change during cyclic loading, which was not investigated in this work. However, the plastic strain amplitudes measured during the fatigue tests were extremely small, i.e., at the resolution limit of the extensometer used of 0.8 µm, which is in accordance with the work of Awd et al. for the AB condition.[44] So the residual stresses are supposed to be roughly stable. Therefore, Equation (3) was used to estimate the influence of residual stresses on $\sigma_{w,Nog.}$, leading to changes in the $\sigma_a/\sigma_{w,Nog.}$-N_f curves, which is illustrated in **Figure 8**. Considering the residual stresses, the two heat-treated variants now show nearly identical values of $\sigma_a/\sigma_{w,Nog.}$, and thus, the differences observed between the SR and T6 condition are expected to be mainly caused by the different defect sizes and residual stresses at the surface. However, in Figure 8, the AB condition still reveals the smallest $\sigma_a/\sigma_{w,Nog.}$ and hence shows a significantly lower defect tolerance than the heat-treated conditions. Consequently, the improved fatigue strength of the T6 and SR condition in relation to the "as-built" variant is assumed to be mainly caused by an improved defect tolerance.

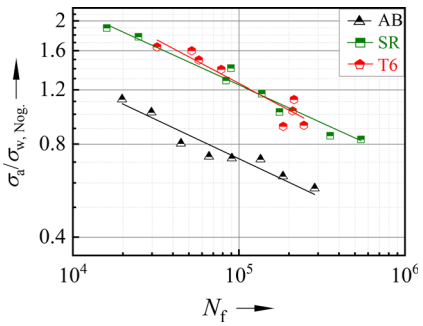

Figure 8. $\sigma_a/\sigma_{w,Nog.}$-N_f curves determined for the specimens of the different conditions investigated, considering the initial process-induced residual stresses.

To underpin these hypotheses, CIT were performed to characterize the cyclic hardening potential, which correlates with the defect tolerance of a material as demonstrated in previous work.[13,22] The $h_{a,p}$-N curves obtained in the CIT show pronounced differences in the cyclic deformation behavior of the different conditions (see **Figure 9**a). For the T6 and SR variants, significantly steeper slopes of the $h_{a,p}$-N curves are observed than for the AB variant, which indicates stronger cyclic hardening. Consequently, these conditions exhibit higher $|e_{II}|$ (see Figure 9b), which supports the hypothesis of an increased defect tolerance after both considered heat treatments, which corresponds to the higher plastic deformability of heat-treated variants than the as-built condition as observed by Fernandes et al. in push–pull fatigue tests.[45]

Comparing the results obtained in CIT at the T6 and SR conditions, only a slightly higher cyclic hardening potential was observed after artificial aging. Nevertheless, this indicates a higher defect tolerance of the T6 variant, which is not supported by the $\sigma_a/\sigma_{w,Nog.}$-N_f curves shown in Figure 8. Note that for an evaluation of the defect tolerance, besides the cyclic hardening potential also the plastic deformability of a material must be considered.[22] As shown in Figure 9a, the SR condition reveals higher $h_{a,p}$, which indicates a more pronounced plastic deformation in CIT and correlates with the higher elongation at fracture A obtained in tensile tests (see Figure 4 and Table 3). It is, hence, assumed that the superimposition of the difference in cyclic hardening potential and plastic deformability results in nearly identical defect tolerances of the SR and T6 conditions.

In addition to the cyclic deformation behavior, the CIT enabled the determination of the hardness in the failure relevant surface-near area. The microhardness determined in this region

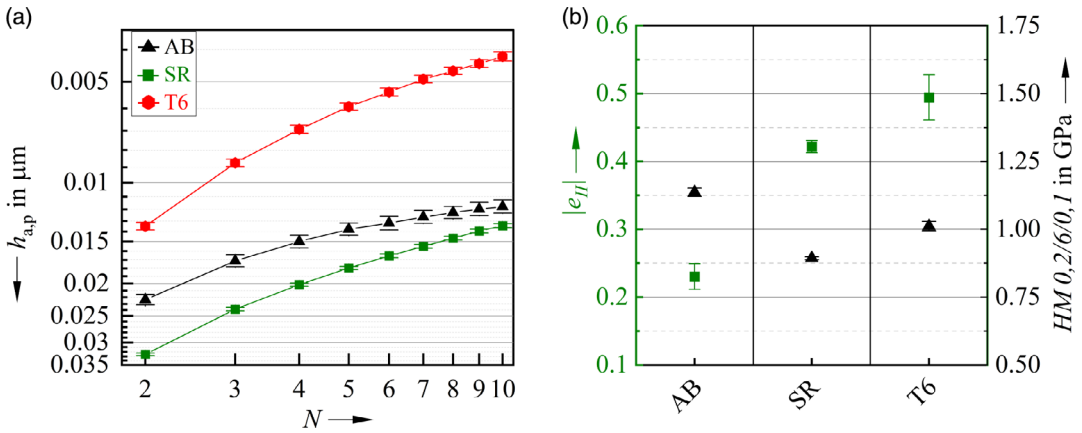

Figure 9. a) $h_{a,p}$-N curves as well as b) cyclic hardening exponent$_{CHT}$ $|e_{II}|$ and Martens hardness (HM) obtained in cyclic indentation tests in the surface-near area.

correlates to the Vickers hardness in the material volume (compare Table 3 and Figure 9b), and thus, the effects of local differences in the hardness are excluded.

In summary, despite a smaller hardness, the heat-treated variants show an increased fatigue strength, which is caused by a reduction of the tensile residual stresses but mainly by an improved defect tolerance. Since additively manufactured materials contain process-induced defects, the defect tolerance of the material volume is crucial for the fatigue life, and an evaluation of the fatigue strength solely based on tensile tests or hardness is insufficient.

Because additively manufactured components exhibit many geometrical notches, both the residual stresses and the materials ability to withstand stress concentrations are of great relevance. Since the applied heat treatments reduce detrimental residual stresses at the surface and improve the defect tolerance, a higher damage tolerance is expected for heat-treated components.

5. Summary and Conclusion

In this work, the influence of two different heat treatments, i.e., stress-relieving (SR) and artificial aging (T6), on the fatigue behavior of additively manufactured specimens made of AlSi10Mg was analyzed. The specimens were manufactured using a PBF-LB. To determine the interrelation of the process-induced notch effects with the material volume properties, near-net shaped specimens with an additively manufactured surface were heat treated and subsequently subjected to tensile and fatigue tests. In addition to the mechanical testing, the changes in the microstructure and the residual stresses caused by the heat treatments were investigated and linked to the respective mechanical properties. From the results obtained, the following conclusions can be drawn: 1) Both heat treatments resulted in a dissolution of the intragranular Si-rich cells, being more pronounced after T6 treatment, which further leads to the formation of precipitates. The microstructural changes caused by the heat treatments led to a decreased hardness and monotonic strength, but a higher cyclic hardening potential, and thus an improved defect tolerance. 2) Despite a lower strength of the material volume, the heat-treated variants show higher fatigue life than the "as-built" condition. This is partially caused by the relatively high tensile residual stresses of the "as-built" condition, which are resolved by the heat treatments. However, the main reason for the higher fatigue strength of T6- and SR-treated material in relation to the "as-built" variant is the improved defect tolerance caused by microstructural changes due to the heat treatments. 3) Comparing the T6 and SR heat treatments, the artificial aging leads to a higher fatigue strength. Besides the smaller defects observed in the T6 specimens, this can be mainly attributed to the compressive residual stresses at the surface induced by the artificial aging. Moreover, the T6 treatment leads to a higher cyclic hardening potential and a higher hardness, which is caused by precipitations. However, as the SR results in a higher ductility, both heat-treated variants reveal a similar defect tolerance. 4) For AlSi10Mg manufactured via PBF-LB, the defect tolerance is crucial for the fatigue strength since the material contains process-induced defects. Consequently, to evaluate the fatigue properties of additively manufactured materials, the strength as well as the defect tolerance must be considered.

Acknowledgements

The specimens analyzed in the presented work were manufactured by the colleagues of the Institute for Mechanical and Automotive Design iMAD (Prof. Dr.-Ing. R. Teutsch, A. Al-Zuhairi, M. Ley) and the Institute for Manufacturing Technology and Production Systems FBK (Prof. Dr.-Ing. J. C. Aurich, Dr.-Ing. B. Kirsch, J. Steiner-Stark) of the RPTU, which is gratefully acknowledged. Moreover, the authors want to thank the priority research program of Rhineland-Palatinate "Advanced Materials Engineering (AME)" for the financial support.

Open Access funding enabled and organized by Projekt DEAL.

Conflict of Interest

The authors declare no conflict of interest.

Data Availability Statement

The data that support the findings of this study are available from the corresponding author upon reasonable request.

Keywords

cyclic indentation tests, defect tolerance, fatigue behavior, heat treatments, laser-based powder bed fusion, process-induced defects

Received: December 21, 2022
Revised: March 28, 2023
Published online: April 25, 2023

[1] J. L. Bartlett, X. Li, *Addit. Manuf.* **2019**, *27*, 131.
[2] W. Schneller, M. Leitner, S. Pomberger, S. Springer, F. Beter, F. Grün, *J. Manuf. Mater. Process.* **2019**, *4*, 89.
[3] P. Ferro, A. Fabrizi, F. Berto, G. Savio, R. Meneghello, S. Rosso, *Theor. Appl. Fract. Mech.* **2020**, *108*, 102611.
[4] T. DebRoy, H. L. Wei, J. S. Zuback, T. Mukherjee, J. W. Elmer, J. O. Milewski, A. M. Beese, A. Wilson-Heid, A. De, W. Zhang, *Prog. Mater. Sci.* **2018**, *92*, 112.
[5] Y. Murakami, H. Masuo, Y. Tanaka, M. Nakatani, *Procedia Struct. Integrity* **2019**, *19*, 113.
[6] Y. Murakami, *Metal Fatigue: Effects of Small Defects and Nonmetallic Inclusions*, Elsevier, Oxford **2002**.
[7] S. Beretta, S. Romano, *Int. J. Fatigue* **2017**, *94*, 178.
[8] R. Konecna, F. Uriati, G. Nicoletto, V. Tibor, *Procedia Struct. Integrity* **2021**, *34*, 135.
[9] Z. Wu, S. Wu, J. Bao, W. Qian, S. Karabal, W. Sun, P. J. Withers, *Int. J. Fatigue* **2021**, *151*, 106317.
[10] S. Romano, A. Brückner-Foit, A. Brandão, J. Gumpinger, T. Ghidini, S. Beretta, *Eng. Fract. Mech.* **2018**, *187*, 165.
[11] M. Bonneric, C. Brugger, N. Saintier, *Int. J. Fatigue* **2020**, *134*, 105505.
[12] S. Beretta, M. Gargourimotlagh, S. Foletti, A. Du Plessis, M. Riccio, *Int. J. Fatigue* **2020**, *139*, 105737.
[13] B. Blinn, F. Krebs, M. Ley, R. Teutsch, T. Beck, *Int. J. Fatigue* **2020**, *131*, 105301.
[14] H. Masuo, Y. Tanaka, S. Morokoshi, H. Yagura, T. Uchida, Y. Yamamoto, Y. Murakami, *Int. J. Fatigue* **2018**, *117*, 163.

[15] E. Wycisk, A. Solbach, S. Siddique, D. Herzog, F. Walther, C. Emmelmann, *Phys. Proc.* **2014**, *56*, 371.
[16] F. Sausto, C. Tezzele, S. Beretta, *Metals* **2022**, *6*, 898.
[17] J. Tenkamp, S. Stammkötter, M. Merghany, F. Walther, *Addit. Manuf. Lett.* **2022**, *3*, 100076.
[18] J. Tenkamp, F. Stern, F. Walther, *Addit. Manuf. Lett.* **2022**, *3*, 100054.
[19] K. Shiozawa, L. Lu, *Adv. Mater. Res.* **2008**, *44*, 33.
[20] H. S. Kramer, P. Starke, M. Klein, D. Eifler, *Int. J. Fatigue* **2014**, *63*, 78.
[21] B. Blinn, D. Görzen, M. Klein, D. Eifler, T. Beck, *Int. J. Fatigue* **2019**, *119*, 78.
[22] D. Görzen, H. Schwich, B. Blinn, W. Song, U. Krupp, W. Bleck, T. Beck, *Int. J. Fatigue* **2021**, *144*, 106042.
[23] J. N. Domfang Ngnekou, Y. Nadot, G. Henaff, J. Nicolai, L. Ridosz, *Metals* **2021**, *11*, 1432.
[24] M. Muhammad, P. D. Nezhadfar, S. Thompson, A. Saharan, N. Phan, N. Shamsaei, *Int. J. Fatigue* **2021**, *146*, 106165.
[25] N. T. Aboulkhair, I. Maskery, C. Tuck, I. Ashcroft, N. M. Everitt, *Mater. Des.* **2016**, *104*, 174.
[26] S. Bagherifard, N. Beretta, S. Monti, M. Riccio, M. Bandini, M. Guagliano, *Mater. Des.* **2018**, *145*, 28.
[27] A. Tridello, J. Fiocchi, C. A. Biffi, G. Chiandussi, M. Rossetto, A. Tuissi, D. S. Paolino, *Int. J. Fatigue* **2020**, *137*, 105659.
[28] A. Tridello, J. Fiocchi, C. A. Biffi, G. Chiandussi, M. Rossetto, A. Tuissi, D. S. Paolino, *Fatigue Fract. Eng. Mater. Struct.* **2019**, *12*, 2794.
[29] M. T. Di Giovanni, J. T. O. de Menezes, G. Bolelli, E. Cerri, E. M. Castrodeza, *Eng. Fract. Mech.* **2019**, *217*, 106564.
[30] S. Beretta, L. Patriarca, M. Gargourimotlagh, A. Hardaker, D. Brackett, M. Salimian, J. Gumpinger, T. Ghidini, *Mater. Des.* **2022**, *218*, 110713.
[31] N. Takata, H. Kodaira, K. Sekizawa, A. Suzuki, M. Kobashi, *Mat. Sci. Eng., A* **2017**, *704*, 218.
[32] M. Fousová, D. Dvorský, A. Michalcová, D. Vojtěch, *Mater. Charact.* **2018**, *137*, 119.
[33] J. Wu, X. Q. Wang, W. Wang, M. M. Attallah, M. H. Loretto, *Acta Mater.* **2016**, *117*, 311.
[34] L. Zhao, J. G. Santos Macías, L. Ding, H. Idrissi, A. Simar, *Mat. Sci. Eng., A* **2019**, *764*, 138210.
[35] DIN EN ISO 25178-2:2012-09, Geometrische Produktspezifikation (GPS)_- Oberflächenbeschaffenheit: Flächenhaft_- Teil_2: Begriffe Und Oberflächen-Kenngrößen (ISO_25178-2:2012); EN_ISO_25178-2:2012, Berlin.
[36] DIN EN ISO 6892-1:2020-06, Metallische Werkstoffe_- Zugversuch_- Teil_1: Prüfverfahren Bei Raumtemperatur (ISO_6892-1:2019); EN_ISO_6892-1:2019, Berlin.
[37] H. Noguchi, K. Morishige, T. Fujii, T. Kawazoe, S. Hamada, in *Proc. 56th JSMS Annual Meetings* **2007**, p. 137.
[38] N. E. Uzan, R. Shneck, O. Yeheskel, N. Frage, *Mater. Sci. Eng., A* **2017**, *704*, 229.
[39] S. Leuders, T. Lieneke, S. Lammers, T. Tröster, T. Niendorf, *J. Mater. Res.* **2014**, *17*, 1911.
[40] E. Brandl, U. Heckenberger, V. Holzinger, D. Buchbinder, *Mater. Des.* **2012**, *34*, 159.
[41] J. N. Domfang Ngnekou, Y. Nadot, G. Henaff, J. Nicolai, W. H. Kan, J. M. Cairney, L. Ridosz, *Int. J. Fatigue* **2019**, *119*, 160.
[42] U. Zerbst, M. Vormwald, R. Pippan, H.-P. Gänser, C. Sarrazin-Baudoux, M. Madia, *Eng. Fract. Mech.* **2016**, *153*, 190.
[43] M. Cremer, M. Zimmermann, H.-J. Christ, *Int. J. Fatigue* **2013**, *57*, 120.
[44] M. Awd, F. Stern, A. Kampmann, D. Kotzem, J. Tenkamp, F. Walther, *Metals* **2018**, *10*, 825.
[45] R. F. Fernandes, J. S. Jesus, R. Branco, L. P. Borrego, J. D. Costa, J. Ferreira, *Int. J. Fatigue* **2022**, *164*, 107157.